

**MINISTRY OF EDUCATION
AND TRAINING**

**VIETNAM ACADEMY OF SCIENCE
AND TECHNOLOGY**

HỌC VIỆN KHOA HỌC VÀ CÔNG NGHỆ



Le Anh Thi

**PEROVSKITE $\text{Cs}_2\text{SnCl}_{6-x}\text{Br}_x$ ($x = 0, 1, 2, 3, 4, 5, 6$):
SYNTHESIS, PHONON DYNAMICS, AND OPTICAL
PROPERTIES**

**SUMMARY OF DISSERTATION ON
SCIENCES OF MATTER**

Major: Materials for Electronics

Code: **9 44 01 23**

Hanoi - 2025

The dissertation is completed at: Graduate University of Science and Technology, Vietnam Academy Science and Technology

Supervisors:

- 1. Supervisor 1: Dr. Man Minh Tan, Ton Duc Thang University
- 2. Supervisor 2: Dr. Đò Thi Anh Thu, Institute of Materials Science, Vietnam Academy Science and Technology

Referee 1:

Referee 2:

Referee 3:

The dissertation is examined by Examination Board of Graduate University of Science and Technology, Vietnam Academy of Science and Technology at..... (time, date.....)

The dissertation can be found at:

- 1. Graduate University of Science and Technology Library
- 2. National Library of Vietnam

INTRODUCTION

1. The urgency of the thesis

Halide metal perovskite semiconductors (MHPs) have been extensively studied due to their outstanding optoelectronic properties. However, lead-based MHPs raise concerns regarding toxicity and stability for practical device applications. Replacing lead with safer metals such as tin presents challenges in maintaining optical performance, as Sn^{2+} ions are easily oxidized to Sn^{4+} . The investigation of Cs_2SnX_6 ($X = \text{Cl}, \text{Br}$) crystals, which exhibit broad-band emission and retain optical properties through self-trapped exciton states, offers a promising solution to the issues of toxicity and stability, while unlocking new application potentials in optoelectronics. Therefore, studying Cs_2SnX_6 ($X = \text{Cl}, \text{Br}$) perovskite materials is of great significance and urgency in the development of new optoelectronic materials.

2. Research objectives of the thesis

Successfully synthesized a series of mixed-halide double perovskite crystals $\text{Cs}_2\text{SnCl}_{6-x}\text{Br}_x$ ($x = 0, 1, 2, 3, 4, 5, 6$) with varying halogen substitution ratios.

Clarified the influence of halide composition on the band gap energy, optical properties, and lattice vibrational characteristics of $\text{Cs}_2\text{SnCl}_{6-x}\text{Br}_x$ crystals.

Elucidated the optical transition mechanism and the formation of self-trapped exciton states in Cs_2SnBr_6 crystals.

3. Main research contents of the thesis

Synthesized $\text{Cs}_2\text{SnCl}_{6-x}\text{Br}_x$ ($x = 0, 1, 2, 3, 4, 5, 6$) samples according to the designed composition.

Performed theoretical calculations and analyzed the vibrational and electrical properties of Cs_2SnX_6 ($X = \text{Cl}, \text{Br}$) crystals.

Investigated the structural characteristics and optical transition processes of Cs_2SnX_6 ($X = \text{Cl}, \text{Br}$) samples.

Investigated the structural characteristics and optical transition processes of $\text{Cs}_2\text{SnCl}_{6-x}\text{Br}_x$ ($x = 0, 1, 2, 3, 4, 5, 6$) crystal structures.

CHAPTER 1. OVERVIEW OF METAL-HALIDE PEROVSKITE MATERIALS

1.1. Crystal Structure of Perovskite Materials

The perovskite structure has the formula ABX_3 , where the A cation is located at the corners of the cubic unit cell, the B cation at the body center, and the X anion at the face centers (Figure 1.1).

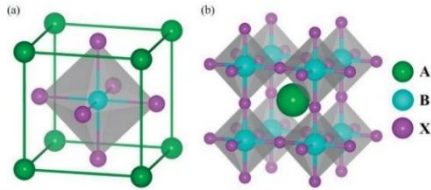


Figure 1.1. Crystal structure of perovskite ABX_3 : (a) crystal structure in the unit cell; (b) supercell consisting of 8 BX_6 octahedra at the vertices.

1.2. Structural Characteristics of Metal-Halide Perovskite Materials

Metal halide perovskite (MHP) crystals have a structure similar to oxide perovskites ABX_3 , in which the A site is typically occupied by monovalent metal ions or organic molecules. The B site is occupied by divalent metal cations.

1.3. Optical Properties of Metal Perovskite Materials

1.3.1. Optical Properties of Lead-Halide Perovskite Materials

Lead-halide perovskite (LHP) materials with the formula $APbX_3$ exhibit high efficiency due to their superior optoelectronic properties, such as large light absorption coefficients, high electron and hole mobilities, long carrier lifetimes, large carrier diffusion lengths, low carrier trap densities, small exciton binding energies, and low Urbach energies. These properties enhance the performance and stability of optoelectronic devices (Figure 1.17). However, the presence of Pb in LHP materials has impacts on human health and the environment (Figure 1.18).

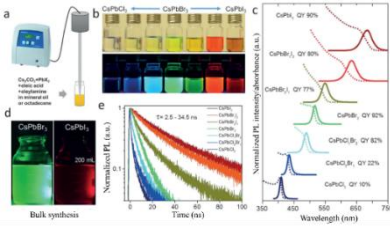


Figure 1.2. a) Ultrasonic method for synthesizing CsPbX_3 , b) Photographs of CsPbX_3 colloidal solutions under sunlight (top) and 367 nm UV light (bottom), c) UV/Vis and PL spectra and PLQY, d) CsPbBr_3 and CsPbI_3 samples under UV light, e) fluorescence decay kinetics.

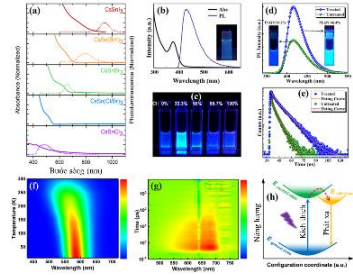


Figure 1.3. Schematic illustration of the impacts of Pb in LHP materials.

1.3.2. Optical Properties of Lead-Free Halide Perovskites

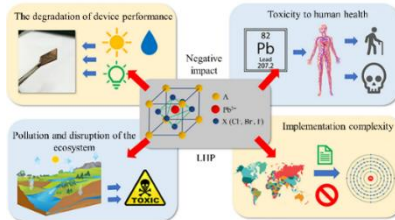


Figure 1.4. (a-b) Absorption and PL spectra of CsSnX_3 , and $(\text{CH}_3\text{NH}_3)_3\text{Bi}_2\text{Br}_9$, (c) $(\text{CH}_3\text{NH}_3)_3\text{Bi}_2(\text{Cl}/\text{Br})_9$ QDs under UV light, (d) PL spectra of $\text{Cs}_3\text{Bi}_2\text{Br}_9$ QDs with and without water treatment, (e) Time-resolved PL decay of $\text{Cs}_3\text{Bi}_2\text{Br}_9$ QDs with and without water treatment, (f) Temperature-dependent PL spectra pseudocolor map of CsCu_2I_3 , (g) Transmission-absorption pseudocolor map of CsCu_2I_3 film, (h) Schematic diagram of the STE dynamics process of CsCu_2I_3 .

Lead-free halide perovskite (LFHP) materials are attracting attention due to their higher stability and safety compared to LHP materials. Replacing

divalent lead ions with a pair of trivalent and monovalent cations has created a double perovskite structure, with twice the number of unit cells compared to LHP CsPbX_3 . LFHP crystals such as A_2SnI_6 ($\text{A} = \text{Cs}, \text{MA}$), Cs_2PdB_6 , and Cs_2TiBr_6 are being investigated in the field of optoelectronics due to their unique optical properties, holding promise for replacing LHPs in optoelectronic applications.

1.3.3. Optical Properties of Tin-Halide Perovskites

Tin-halide perovskites (THPs) are a promising alternative to lead-halide perovskites (LHPs) because tin (Sn) has a similar electron configuration and ionic radius to lead, enabling THP nanocrystals to maintain optoelectronic properties similar to LHPs. Another key advantage is that Sn can decompose into non-toxic SnO_2 upon contact with water and air, aligning with the trend of developing environmentally friendly materials (Fig. 1.25).

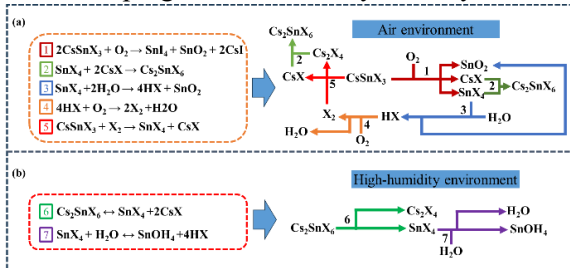


Figure 1.5. (a) Cyclic degradation mechanism of CsSnX_3 NCs in air, (b) Cyclic degradation mechanism of Cs_2SnX_6 NCs in a high-humidity environment.

In terms of optics and electronics, THP NCs have a high absorption coefficient, long lifetimes, and good carrier mobility. Notably, because Sn has a higher electronegativity than Pb, THPs generally have a narrower band gap, approximately 1.2 eV. Electron-phonon interactions not only increase the deformability of the crystal lattice but also create transient excited states (STEs), emitting light with a broad spectral band and a large Stokes shift upon recombination. Understanding the formation and development of STEs is crucial for optimizing the performance of devices based on Cs_2SnBr_6 NCs,

opening up potential applications in light-emitting devices, sensors, and solar energy.

1.4. Applications of Lead-Free Metal-Halide Perovskites

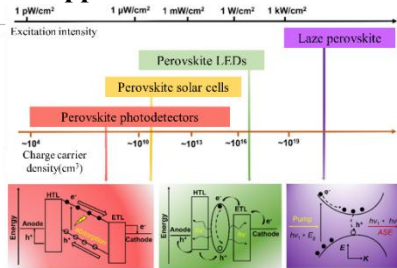


Figure 1.6. The nature of excitons/charge carriers in PeNC materials and photophysical processes in various optoelectronic devices.

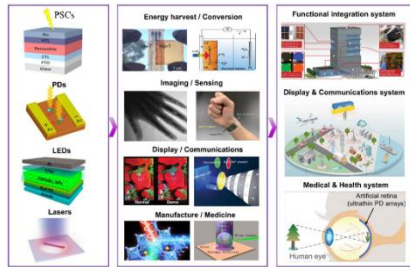


Figure 1.7. The scientific and technological revolution from the materials and photophysical optoelectronic applications of PeNC MHP.

CHAPTER 2. RESEARCH METHODS AND TECHNIQUES

2.1. Materials Synthesis Methods

2.1.1. Chemicals and Reaction Conditions

2.1.2. Synthesis of Cs_2SnX_6 ($X = Cl, Br$) using the Hydrothermal Method

The hydrothermal method has been used to synthesize Cs_2SnX_6 ($X = Cl, Br$) nanocrystals (NCs), with the process illustrated in Figure 2.1.



Figure 2.1. Schematic diagram of the Cs_2SnX_6 ($X = Cl, Br$) synthesis.

2.1.3. Synthesis of $Cs_2SnCl_{6-x}Br_x$ ($x = 0, 1, 2, 3, 4, 5, 6$) perovskite crystal

The fabrication of $\text{Cs}_2\text{SnCl}_{6-x}\text{Br}_x$ ($x = 0, 1, 2, 3, 4, 5, 6$) crystals with varying halide compositions was carried out by rapidly injecting a precursor solution of SnX_4 ($X = \text{Cl}, \text{Br}$) with different x values into a Cs^+ -containing solution at 140°C , as illustrated in the schematic shown in Figure 2.2.

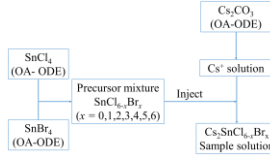


Figure 2.2. Schematic diagram of the $\text{Cs}_2\text{SnCl}_{6-x}\text{Br}_x$ ($x = 0, 1, 2, 3, 4, 5, 6$) material fabrication steps.

2.1.4. Selection of Fabrication Temperature

2.2. Techniques for Analyzing the Structure and Properties of Materials

2.2.1. Techniques for Analyzing Morphological Structure

2.2.2. Energy-Dispersive Spectroscopy Method

2.2.3. Crystal Structure Analysis

2.2.4. Vibrational Spectroscopy Method

2.2.5. Spectroscopic Characterization

2.2.6. Fluorescence Lifetime

2.3. Calculation Methods

CHAPTER 3. STRUCTURAL AND OPTICAL PROPERTY

INVESTIGATION OF Cs_2SnX_6 ($X = \text{Cl}, \text{Br}$) CRYSTALS

3.1. Crystal structure and Morphology of Cs_2SnX_6 ($X = \text{Br}, \text{Cl}$) crystals

3.1.1. Characteristics of the crystal structure

In Cs_2SnX_6 crystals, the Sn atom is located at the center of the SnX_6 octahedron, surrounded by six X atoms. The unit cell contains eight Cs^+ cations and four $[\text{SnX}_6]^{2-}$ anions at the corners and face centers, as illustrated in Figure 3.1.

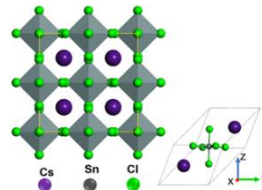


Figure 3.1. Illustration of the structure and unit cell of Cs_2SnX_6 ($X = \text{Cl}, \text{Br}$) crystals.

The XRD analysis results of Cs_2SnX_6 ($X = \text{Cl}, \text{Br}$) presented in Figures 3.2 and 3.3, show clearly defined diffraction peaks, confirming that both samples possess a cubic structure belonging to the $Fm\bar{3}m$ space group. The Cs_2SnCl_6 sample (Figure 3.2) exhibits diffraction peaks at angles of 13.5° , 23.6° , 29.7° , 33.4° , 36.6° , 41.2° , 43.7° , 47.8° , 50.1° , 53.9° , 56.7° , and 59.4° , corresponding to the Miller indices (111), (220), (331), (222), (400), (331), (422), (511), (440), (533), (620), and (622), respectively.

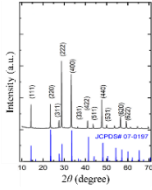


Figure 3.2. X-ray diffraction pattern of Cs_2SnCl_6 samples.

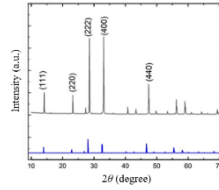


Figure 3.3. X-ray diffraction pattern of the Cs_2SnBr_6 sample.

The Cs_2SnBr_6 sample (Figure 3.3) displays diffraction peaks corresponding to the crystal planes (111), (220), (222), (400), (422), (440), (622), and (444) at diffraction angles of 14.3° , 23.4° , 28.6° , 33.1° , 40.9° , 47.5° , 56.4° , and 59.3° , respectively. The lattice constants of the Cs_2SnX_6 ($X = \text{Cl}, \text{Br}$) samples are 10.3 \AA (Cs_2SnCl_6) and 10.7 \AA (Cs_2SnBr_6), respectively. Table 3.1 compares the obtained lattice constants in this study with previously reported values, thereby confirming the accuracy and reliability of the XRD analysis.

Table 3.1. Lattice parameters and bond lengths of atoms in the structure of Cs_2SnX_6 ($X = \text{Cl}, \text{Br}$) perovskite crystal samples.

Sample	Lattice constant (Å)	$d_{\text{Cs-Cs}}$ (Å)	$d_{\text{Sn-Sn}}$ (Å)	$d_{\text{Cs-Sn}}$ (Å)	$d_{\text{Cs-X}}$ (Å)	$d_{\text{Sn-X}}$ (Å)	$d_{\text{X-X}}$ (Å)	$d_{\text{Sn-X}}$ CsSnX_3 (Å) [89]
	10,3;							
Cs_2SnCl_6	10,39 ^a ; 10,39 ^b ; 10,38 ^c 10,7;	10,3	4,46	3,48	3,41	3,41;	2,48 ^c	2,75
Cs_2SnBr_6	10,74 ^b ; 10,83 ^c ; 10,86 ^d	10,7	4,66	3,68	3,54	3,54;	2,61 ^c	2,94

^a[149], ^b[130], ^c[89], ^d[150].

3.1.2. Characteristics of the Morphology

The SEM image of the Cs_2SnCl_6 sample (Figure 3.4) shows that the particles have an octahedral shape with an average size of approximately $1.5 \mu\text{m}$. The elemental distribution within the Cs_2SnCl_6 crystal was analyzed using EDX spectroscopy (Figure 3.5).

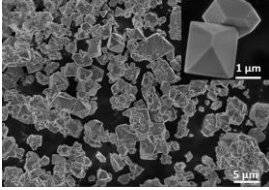


Figure 3.4. SEM image of the Cs_2SnCl_6 sample.

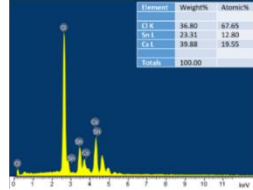


Figure 3.5. EDX spectrum of the Cs_2SnCl_6 crystal sample.

The SEM image of the Cs_2SnBr_6 sample (Figure 3.6(a)) shows that the sample has an octahedral shape with an average particle size of approximately $3 \mu\text{m}$. The HRTEM image and FFT of the sample (Figures 3.6(b) and (c)) show the (222) lattice plane with a spacing of $d = 0.33 \text{ nm}$. The EDS spectrum analysis results (Figure 3.7) for the Cs_2SnBr_6 sample show the elemental composition: 19.79% Cs, 11.30% Sn, and 68.92% Br.

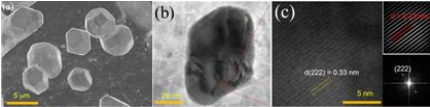


Figure 3.6. (a) SEM image, (b-c) HRTEM image and FFT of the Cs_2SnBr_6 sample.

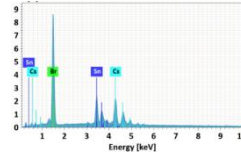


Figure 3.7. EDS spectrum of the Cs_2SnBr_6 crystal.

3.2. Vibrational spectroscopic properties of Cs_2SnX_6 ($X = \text{Cl}, \text{Br}$) crystals

First-principles calculations were applied to compute the phonon dispersion along the symmetry directions in the Cs_2SnX_6 crystal. The unit cell of Cs_2SnCl_6 contains 58 atoms, and its 10 phonon modes at the Brillouin zone center are classified based on the O_h point group symmetry as $\text{A}_{1g} + \text{E}_g + \text{T}_{1g} + 2\text{T}_{2g} + 4\text{T}_{1u} + \text{T}_{2u}$ (Figure 3.8).

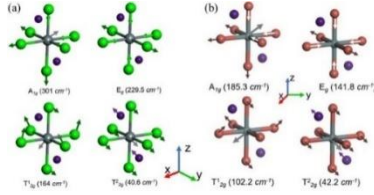


Figure 3.8. Vibrational modes of the (a) Cs_2SnCl_6 and (b) Cs_2SnBr_6 crystals.

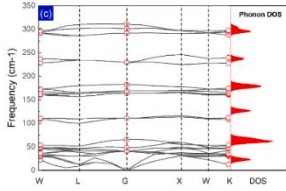


Figure 3.9. Phonon dispersion of the Cs_2SnCl_6 sample.

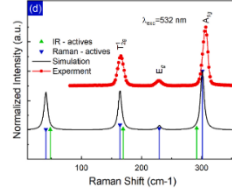


Figure 3.10. Calculated and experimental Raman spectra of the Cs_2SnCl_6 sample.

The calculated phonon dispersion and phonon DOS of the Cs_2SnCl_6 crystal are presented in Figure 3.9. The vibrational characteristics of the Cs_2SnCl_6 sample (Figure 3.10) show vibrational modes with A_{1g} , E_g , and two T_{2g} symmetries. The Raman DOS peaks obtained experimentally were fitted using three Lorentzian functions, showing a small deviation of approximately 5 cm^{-1} from the theoretical values. For the Cs_2SnBr_6 sample, the phonon dispersion is more complex than that of Cs_2SnCl_6 , as shown in Figure 3.11.

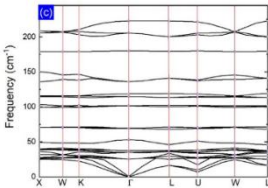


Figure 3.11. Phonon dispersion curve of the Cs_2SnBr_6 crystal.

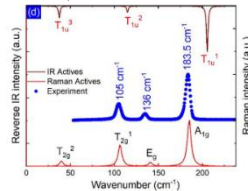


Figure 3.12. Calculated and experimental Raman spectra of the Cs_2SnBr_6 crystal.

Phonon analysis of Cs_2SnBr_6 shows that the T_{1u} mode (208 cm^{-1}) reflects the Sn-Br stretching symmetry and Br-Sn-Br bending (116 cm^{-1}).

The 44.8 cm^{-1} vibration is associated with $[\text{SnBr}_6]^{2-}$ and Cs^+ , while the (42.2 cm^{-1}) and (102.2 cm^{-1}) modes are related to Cs^+ and Br-Sn-Br bending, respectively. The E_g and A_{1g} modes are 141.8 cm^{-1} and 185.3 cm^{-1} .

3.3. Electronic properties of Cs_2SnX_6 ($X = \text{Cl}, \text{Br}$) samples

The band structure of the Cs_2SnCl_6 crystal (Figure 3.14(a)) exhibits a direct band gap (3.56 eV) at the Γ point. The T_{1g} orbital of Cl^- is at the top of the VB, and the A_{1g} orbital from the Sn-Cl overlap is at the bottom of the CB. The DOS shows that the top of the VB is primarily contributed by the Cl ($2p^6$) and Cs ($6s^1$) orbitals, while the bottom of the CB originates from Cl ($2p^6$), Cs ($6s^1$), and Sn ($5s^2, 5p^2$) orbitals (Figure 3.16(a)). The energy band structure and DOS of the Cs_2SnBr_6 sample (Figure 3.15) show a direct band gap (2.93 eV) at the Γ point, with the bottom of the CB from the Sn $5s$ and Br $4p$ orbitals, and the top of the VB from the Br $4p$ (T_{1g}) orbitals. The hybridization between Sn $5s$ and Br $4p$ creates the A_{1g} symmetry (Figure 3.16(b)). The Cs_2SnBr_6 crystal has a narrower band gap than Cs_2SnCl_6 (by approximately 0.63 eV) due to the weaker interaction between Sn^{4+} and Br^- . Figure 3.17 shows the atomic positions and charge distribution, demonstrating the non-uniform interaction within the crystal lattice.

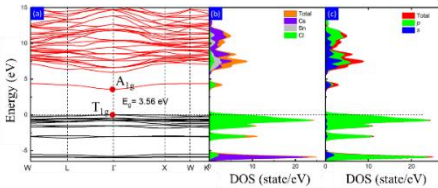


Figure 3.13. (a) Energy band structure, (b, c) total and partial density of states (DOS) of the Cs_2SnCl_6 sample.

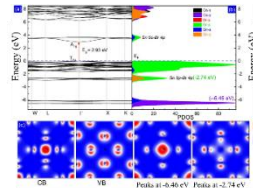


Figure 3.14. (a) Band structure, (b) density of states of the Cs_2SnBr_6 sample, (c) hybridization between the Sn $5s$ and Br $4p$ orbitals with A_{1g} symmetry, and partial charge density of the CB and VB orbitals.

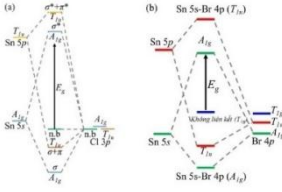


Figure 3.15. The interaction between the Sn and X orbitals in the crystal: (a) Cs_2SnCl_6 ; (b) Cs_2SnBr_6 .

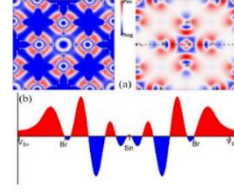


Figure 3.16. (a). Shape of the charge density difference, (b) Vibrational spectrum showing the charge difference.

3.4. Optical Properties of Cs_2SnX_6 ($X = \text{Cl}, \text{Br}$) Perovskite Crystals

The absorption spectra of the Cs_2SnX_6 ($X = \text{Cl}, \text{Br}$) samples (Figure 3.17) do not show a clear exciton absorption peak. The Tauc method was used to determine E_g , as shown in Figure 3.17 (a) for the Cs_2SnCl_6 sample and in the inset of Figure 3.17 (b) for the Cs_2SnBr_6 sample. The band gap (E_g) results for the Cs_2SnX_6 ($X = \text{Cl}, \text{Br}$) samples from Table 3.3 show a small difference between the experimental and theoretical values.

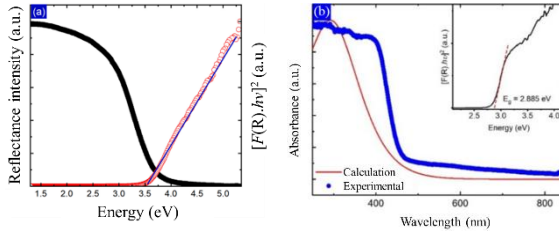


Figure 3.17. UV-Vis diffuse reflectance spectra and Tauc plots for determining the band gap energy of (a) Cs_2SnCl_6 and (b) Cs_2SnBr_6 crystal samples.

Table 3.3. Band gap energy (E_g) of the Cs_2SnX_6 ($X = \text{Cl}, \text{Br}$) samples.

Sample	E_g Experimental (eV)	E_g Calculation (eV)	E_g (Literature Reference) (eV)	Crystal Size (μm) (Literature)
Cs_2SnCl_6	3,55	3,56	3,18 [17];	1,8 [17];
			3,88 [15];	5,0 [15];
			3,9 [89]	4,0 [89].
Cs_2SnBr_6	2,88	2,93	2,7 [89];	2,0 [17];
			2,9 [77].	1-2,0 [77];
				5,1 [89].

The normalized PLE and PL spectra of Cs_2SnX_6 ($X = \text{Cl}, \text{Br}$) nanocrystals are presented in Figures 3.18(a–b). The peak position, full width at half maximum (FWHM), and Stokes shift parameters of the Cs_2SnX_6 ($X = \text{Cl}, \text{Br}$) samples are provided in Table 3.4. The photoluminescence spectral analysis results are listed in Table 3.4. It can be seen that the PLE peak position of the Cs_2SnCl_6 sample is at a wavelength of 336 nm, while for the Cs_2SnBr_6 sample, the PLE peak shifts to a longer wavelength of 428 nm. The PL peak position also shifts from 450 nm (Cs_2SnCl_6) to 522 nm (Cs_2SnBr_6).

Table 3.4. Optical parameter values of the Cs_2SnX_6 samples.

Sample	λ_{PLE} (nm)	λ_{PL} (nm)	Stokes shift (nm)	FWHM (nm)	Huang-Rhys factor S
Cs_2SnCl_6	336	450	114	63	8,96
Cs_2SnBr_6	428	522	91	120	22,3

The difference in Stokes shift between Cl and Br is related to the crystal structure and the interaction between the halogen atoms and the crystal lattice.

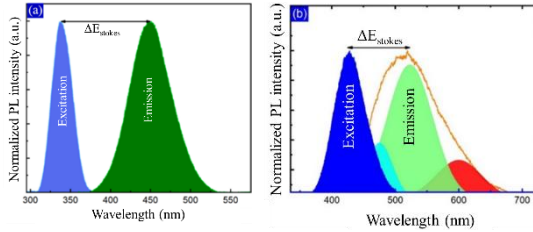


Figure 3.18. Normalized PLE and PL spectra of the (a) Cs_2SnCl_6 and (b) Cs_2SnBr_6 samples.

The Huang-Rhys factor (S) was determined based on the relationship between the Stokes shift energy and the longitudinal optical (LO) phonon frequency using the approximate formula (3.1): $\Delta E_{\text{stokes}} = 2S\hbar\omega_{\text{LO}}$, where S is the Huang-Rhys factor, characterizing the strength of electron–phonon coupling, and $\hbar\omega_{\text{LO}}$ is the energy of the longitudinal optical phonon mode. The Huang–Rhys factors for the Cs_2SnCl_6 and Cs_2SnBr_6 samples are listed in Table 3.4.

3.5. Carrier dynamics and Self-trapped excitons of the Cs_2SnBr_6 crystal

The energy difference between the excited and ground states of the self-trapped exciton (STE) and free exciton configurations is determined by the self-trapping energy E_{STE} and the lattice distortion energy E_d . Where $E_g = 2.88$ eV is the band gap energy; $E_b \approx 320$ meV is the exciton binding energy. Both E_d and E_b can be affected by the arrangement of cations in the lattice structure.

The self-trapping energy E_{STE} and the lattice distortion energy representing the energy difference between the excited and ground states in both self-trapped and free exciton configurations are determined from the configuration coordinate diagram and the estimated Huang–Rhys factors S for these samples, as shown in Figure 3.19.

The PL spectrum of the Cs_2SnBr_6 sample is best fitted with three Gaussian peaks, observed at wavelengths of 475 nm, 522 nm, and 600 nm, corresponding to the luminescence due to band-to-band recombination, exciton luminescence, and luminescence from the STE state.

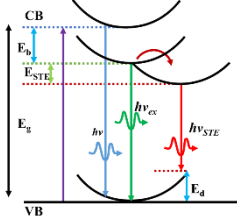


Figure 3.19. Schematic illustration of different internal energy states.

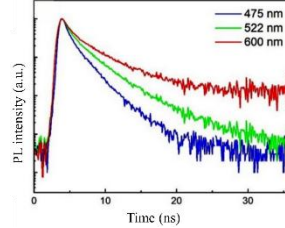


Figure 3.20. Normalized time-resolved PL spectrum of the Cs_2SnBr_6 sample.

The STE states are manifested in the photoluminescence decay spectra at room temperature (Figure 3.20). Longer decay times correspond to lower emission energies, indicating stronger electron–phonon interactions. The PL decay follows an exponential function, confirming the nature of radiative recombination. The fitted lifetimes according to equation (3.8) for emission peaks are: $\tau_{475} = 0.61$ ns, $\tau_{522} = 0.96$ ns, and $\tau_{600} = 1.17$ ns. This suggests that

the formation of STE states in the Cs_2SnBr_6 sample is closely related to strong electron–phonon interactions.

The Huang–Rhys factor of the Cs_2SnBr_6 sample is $S = 22.3$, indicating strong electron–phonon coupling, mainly through Sn–Br vibrations. This interaction traps the hole within the $[\text{SnBr}_6]$ octahedron, alters the electronic configuration of Sn^{4+} , and leads to energy level splitting due to the pseudo-Jahn–Teller effect. This results in a distortion of the octahedral symmetry, which significantly affects the interaction with light.

CHAPTER 4. STRUCTURAL AND OPTICAL PROPERTIES OF $\text{Cs}_2\text{SnCl}_{6-x}\text{Br}_x$ CRYSTALS ($x = 0–6$)

4.1. Structural and Morphological characteristics of $\text{Cs}_2\text{SnCl}_{6-x}\text{Br}_x$ ($x = 0, 1, 2, 3, 4, 5, 6$) crystals

4.1.1. Crystal Structure

Figure 4.1 illustrates the crystal structure of $\text{Cs}_2\text{SnCl}_{6-x}\text{Br}_x$ ($x = 0, 1, 2, 3, 4, 5, 6$) as Cl halogen atoms are gradually substituted by Br.

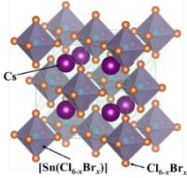


Figure 4.1. Illustration of the crystal structure of the perovskite $\text{Cs}_2\text{SnCl}_{6-x}\text{Br}_x$ crystal.

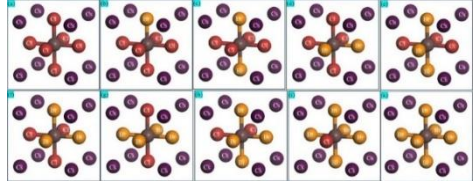


Figure 4.2. Schematic illustration of the crystal structure of $\text{Cs}_2\text{SnCl}_{6-x}\text{Br}_x$ ($x = 0, 1, 2, 3, 4, 5, 6$)

The $\text{Cs}_2\text{SnCl}_{6-x}\text{Br}_x$ ($x = 0, 1, 2, 3, 4, 5, 6$) crystals can exhibit an ordered structure in two possible configurations: symmetric and asymmetric (Figure 4.2). XRD analysis results reveal that all $\text{Cs}_2\text{SnCl}_{6-x}\text{Br}_x$ samples exhibit characteristic diffraction peaks at 2θ angles of 14.3° , 23.4° , 27.4° , 28.7° , 33.2° , and 47.6° , corresponding to the (111), (220), (311), (222), (400), and (440) planes, respectively. These diffraction peak positions are consistent with the crystal phases of both the initial and final

compositions, namely Cs_2SnCl_6 (sample S0) and Cs_2SnBr_6 (sample S6), as referenced by the ICSD card #07-0197.

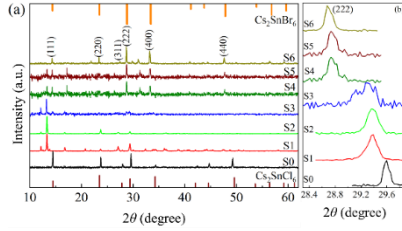


Figure 4.3. (a) XRD patterns, and (b) (222) diffraction peaks of $\text{Cs}_2\text{SnCl}_{6-x}\text{Br}_x$ ($x = 0, 1, 2, 3, 4, 5, 6$) samples.

The samples are identified as single-phase and crystallize in the cubic space group Fm-3m. The bond lengths of atomic pairs as presented in Figure 4.5 and Table 4.1.

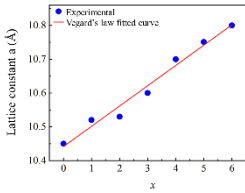


Figure 4.5. The variation of lattice constant values as a function of composition x for $\text{Cs}_2\text{SnCl}_{6-x}\text{Br}_x$ ($x = 0, 1, 2, 3, 4, 5, 6$) samples.

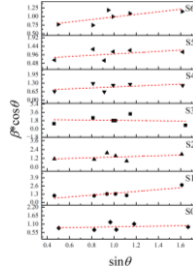


Figure 4.6. The relationship between $\beta \cdot \cos\theta$ and $\sin\theta$ for samples S0 to S6.

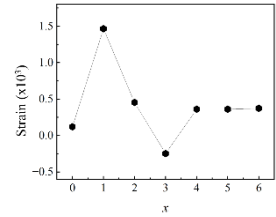


Figure 4.7. Stress variation of $\text{Cs}_2\text{SnCl}_{6-x}\text{Br}_x$ ($x = 0, 1, 2, 3, 4, 5, 6$) samples.

The characteristic crystallographic parameters of the samples presented in Table 4.1 indicate that the unit cell volume increases from 1143.8 \AA^3 (sample S0) to 1259.7 \AA^3 (sample S6). The lattice constant varies with the composition x following an almost linear relationship, as shown in Figure 4.5. The strain (σ) is determined from the slope of the linear plot representing the dependence of β on θ (Figure 4.6). The variation of strain with respect to the composition x is illustrated in Figure 4.7.

Table 4.1. Structural parameters of $\text{Cs}_2\text{SnCl}_{6-x}\text{Br}_x$ ($x = 0, 1, 2, 3, 4, 5, 6$) samples (S0–S6).

Sample	Unit cell volume (\AA^3)	Sn–X bond length (\AA)	Cs–X bond length (\AA)	Sn–Sn bond length (\AA)
S0	1143.8	5.22	3.69	7.39
S1	1164.9	5.26	3.71	7.43
S2	1168.0	5.26	3.72	7.44
S3	1190.2	5.30	3.75	7.49
S4	1224.4	5.35	3.78	7.56
S5	1243.9	5.38	3.80	7.60
S6	1259.7	5.40	3.81	7.63

4.1.2. Morphological Characteristics

SEM images of the $\text{Cs}_2\text{SnCl}_{6-x}\text{Br}_x$ ($x = 0, 1, 2, 3, 4, 5, 6$) samples (Figure 4.8) reveal that the particles exhibit an octahedral morphology with an average size of approximately $1.8 \mu\text{m}$. The substitution of Cl^- ions with Br^- does not affect the shape or size of the samples. The EDS spectra results of samples from S0 to S6 (Figure 4.9) confirm the successful doping process and the substitution between ions, with the Cl^- to Br^- replacement ratios presented in Table 4.3.

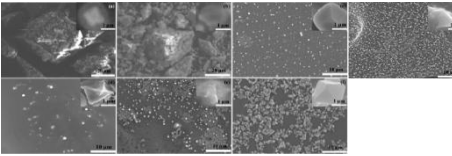


Figure 4.8. SEM images of $\text{Cs}_2\text{SnCl}_{6-x}\text{Br}_x$ ($x = 0, 1, 2, 3, 4, 5, 6$) crystals.

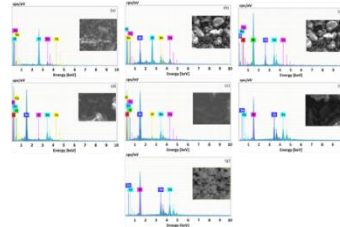


Figure 4.9. EDS images of the $\text{Cs}_2\text{SnCl}_{6-x}\text{Br}_x$ ($x = 0, 1, 2, 3, 4, 5, 6$)

Samples	Cs	Sn	Cl	Br	x
S0	25,62	13,52	60,86	0	0
S1	19,2	10,05	60,93	9,82	0,83
S2	14,1	7,2	62,4	16,3	1,24
S3	27,6	16,1	31,34	24,96	2,66
S4	23,14	13,08	24,94	38,84	3,65
S5	13,1	7,3	24,8	54,8	4,1
S6	18,8	10,6	0	70,6	6

Table 4.3. Chemical composition of the $\text{Cs}_2\text{SnCl}_{6-x}\text{Br}_x$ ($x = 0, 1, 2, 3, 4, 5, 6$) samples obtained from EDS spectra.

4.2. Vibrational Properties

The Raman spectra of $\text{Cs}_2\text{SnCl}_{6-x}\text{Br}_x$ ($x = 0, 1, 2, 3, 4, 5, 6$) samples are presented in Figure 4.10, with the vibrational peak positions determined by Lorentzian fitting listed in Table 4.4. Notably, in samples S1, S2, and S3, additional Raman peaks appear at approximately 271.9 cm^{-1} , 263.6 cm^{-1} , and 252.5 cm^{-1} , respectively—these are located near the most intense peak corresponding to the $\nu(\text{A}_{1g})$ vibrational mode (Figure 4.11).

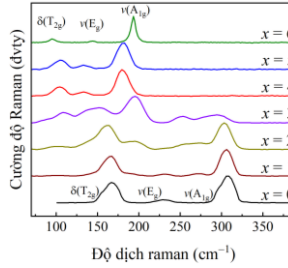


Figure 4.10. Raman spectra of $\text{Cs}_2\text{SnCl}_{6-x}\text{Br}_x$ samples ($x = 0, 1, 2, 3, 4, 5, 6$).

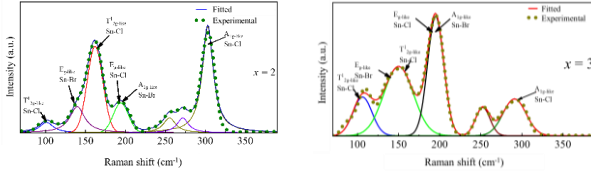


Figure 4.11. Raman spectrum fitting curves of samples S2 and S3.

Table 4.4. Raman-active vibrational mode frequencies of $\text{Cs}_2\text{SnCl}_{6-x}\text{Br}_x$ ($x = 0, 1, 2, 3, 4, 5, 6$) crystals (units: cm^{-1}).

S0	S1	S2	S3	S4	S5	S6	Vibrational Mode	Vibration Type
		100,4	106,1					
166,6	165	160	150	103,7	104,5	95,61	$\delta(\text{T}_{2g})$	Bending vibration of asymmetric X–Sn–X bond
230,4	231,2	196,8	195,2	134	135	144	$\nu(\text{E}_g)$	Stretching vibration of asymmetric Sn–X bond
	272	263,6	252,4					Symmetric stretching vibration of Sn–X
306,8	305,7	303,1	291,1	180,5	181	193,4	$\nu(\text{E}_g)$	

4.3. Optical Properties

4.3.1. Absorption Spectra

The UV–vis absorption spectra of the $\text{Cs}_2\text{SnCl}_{6-x}\text{Br}_x$ ($x = 0, 1, 2, 3, 4, 5, 6$) samples are shown in Figure 4.12. The results indicate that as the Br content increases, the absorption edge gradually shifts toward longer wavelengths, corresponding to a decrease in the optical band gap of the material. Specifically, upon substituting Br for Cl, the band gap energy decreases from 3.55 eV for sample S0 to 3.32 eV for sample S6.

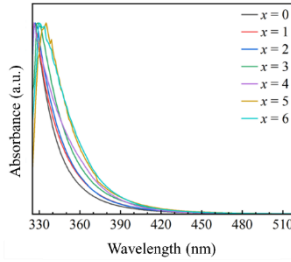


Figure 4.12. Absorption spectra of $\text{Cs}_2\text{SnCl}_{6-x}\text{Br}_x$ ($x = 0, 1, 2, 3, 4, 5, 6$) samples.

4.3.2. Band Gap Engineering

The optical band gap energy (E_g) of the $\text{Cs}_2\text{SnCl}_{6-x}\text{Br}_x$ ($x = 0, 1, 2, 3, 4, 5, 6$) samples was determined from the UV–vis absorption spectra using the Tauc plot method, and the results are presented in Figure 4.13.

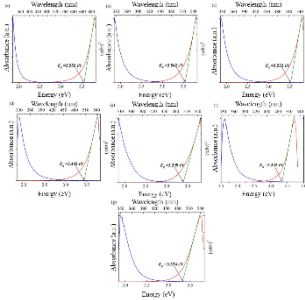


Figure 4.13. Absorption Spectra and Tauc Plots of the samples (a) S0, (b) S1, (c) S2, (d) S3, (e) S4, (f) S5, (g) S6.

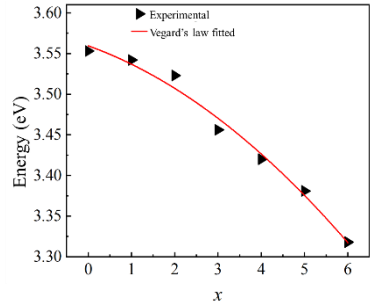


Figure 4.14. Variation of the band gap energy of $\text{Cs}_2\text{SnCl}_{6-x}\text{Br}_x$ ($x = 0, 1, 2, 3, 4, 5, 6$).

The band gap energy (E_g) exhibits a non-linear variation with increasing Br content. This variation is described by the band gap bowing parameter (b), which was determined to be -0.12 .

4.3.3. Photoluminescence and Photoluminescence excitation spectra

The PL and PLE spectra measured at excitation wavelengths of 390 nm and 500 nm (Figure 4.15) show a clear shift in both the emission and excitation peaks as the Br content increases, indicating changes in the electronic structure of the material. The peak positions, FWHM, and Stokes shifts are summarized in Table 4.5.

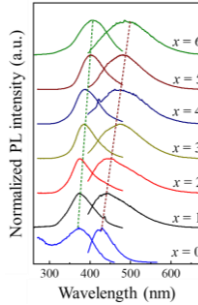


Figure 4.15. PL and PLE Spectra of the $\text{Cs}_2\text{SnCl}_{6-x}\text{Br}_x$ ($x = 0, 1, 2, 3, 4, 5, 6$) samples.

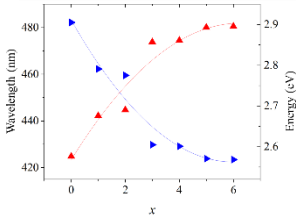


Figure 4.16. Variation of the Emission Peak Position of the $\text{Cs}_2\text{SnCl}_{6-x}\text{Br}_x$ ($x = 0, 1, 2, 3, 4, 5, 6$) samples.

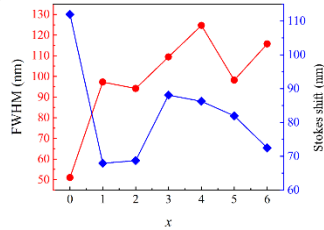


Figure 4.17. Variation of the Stokes Shift and FWHM of the PL Spectra of the $\text{Cs}_2\text{SnCl}_{6-x}\text{Br}_x$ ($x = 0, 1, 2, 3, 4, 5, 6$) samples.

Figure 4.17 illustrates the variation trends of FWHM and Stokes shift as a function of Br content. The results show that the FWHM gradually increases from 50.9 nm ($x = 0$) to 115.7 nm ($x = 6$), reflecting the broadening

of the emission spectrum with increasing Br content. Meanwhile, the Stokes shift decreases from 111.9 nm ($x = 0$) to 72 nm ($x = 6$), indicating changes in the energy transfer mechanism and electronic structure as the halogen composition varies. At higher Br content, the interaction between Br and Sn atoms becomes weaker, resulting in reduced energy loss and a smaller Stokes shift.

Table 4.5. Characteristic Parameters of the PL and PLE Peak Positions, FWHM, and Stokes Shift from the PL and PLE Spectra of the $\text{Cs}_2\text{SnCl}_{6-x}\text{Br}_x$ ($x = 0, 1, 2, 3, 4, 5, 6$) samples.

Content x	λ_{PL}		λ_{PLE}		FWHM		Stokes shift	
	nm	eV	nm	eV	nm	eV	nm	eV
0	424.7	2.91	312.7	3.95	50.9	0.38	111.9	1.04
1	442.1	2.79	374.2	3.29	97.2	0.60	67.9	0.51
2	444.6	2.77	375.9	3.28	94.1	0.58	68.7	0.51
3	473.7	2.61	385.6	3.19	109.4	0.62	88.0	0.59
4	474.4	2.60	388.1	3.17	124.6	0.70	86.2	0.58
5	480.0	2.57	398.1	3.09	98.1	0.59	81.9	0.53
6	480.4	2.56	407.9	3.02	115.7	0.69	72.4	0.46

4.3.4. Color Coordinates and Photoluminescence Decay Time:

The change in photoluminescence color of the $\text{Cs}_2\text{SnCl}_{6-x}\text{Br}_x$ ($x = 0, 1, 2, 3, 4, 5, 6$) samples is demonstrated through the shift of CIE color coordinates. The color coordinate of sample S0 ($x = 0$) is (0.15, 0.035), corresponding to a sky-blue emission, which shifts to (0.20, 0.29) for sample S6 ($x = 6$), indicating a greenish emission. This shift reflects the impact of Cl^- to Br^- substitution in the crystal lattice, as illustrated in Figure 4.17. The time-resolved photoluminescence (TRPL) spectra of the $\text{Cs}_2\text{SnCl}_{6-x}\text{Br}_x$ ($x = 0, 1, 2, 3, 4, 5, 6$) samples are presented in Figure 4.18, with decay parameters extracted by fitting the spectra to a bi-exponential function. The results in Table 4.6 show that the average lifetimes of the samples range from 1.78 ns to 2.82 ns, with sample S3 exhibiting the longest average lifetime (2.82 ns), indicating more stable and prolonged luminescence.

The decay rate constant (k) of the $\text{Cs}_2\text{SnCl}_{6-x}\text{Br}_x$ ($x = 0, 1, 2, 3, 4, 5, 6$) samples was calculated to evaluate their luminescence capability. The decay

rate constant is inversely proportional to the average lifetime τ_{avg} , reflecting the optical stability. Sample S3 has a decay rate of 3.54 ns^{-1} and an average lifetime of 2.82 ns, demonstrating prolonged emission and good optical stability.

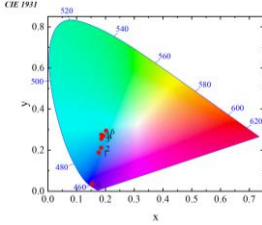


Figure 4.19. CIE Chromaticity Diagram of the $\text{Cs}_2\text{SnCl}_{6-x}\text{Br}_x$ ($x = 0, 1, 2, 3, 4, 5, 6$) samples.

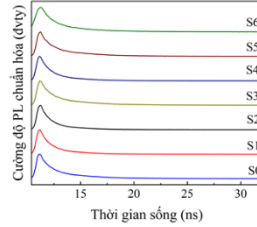


Figure 4.20. Fluorescence Decay Curves of the $\text{Cs}_2\text{SnCl}_{6-x}\text{Br}_x$ ($x = 0, 1, 2, 3, 4, 5, 6$) samples.

Table 4.5. Lifetime Parameter and Decay Rate Values for the $\text{Cs}_2\text{SnCl}_{6-x}\text{Br}_x$ ($x = 0, 1, 2, 3, 4, 5, 6$) samples.

Samples	τ_1 (ns)	τ_2 (ns)	τ_{th} (ns)	k (ns^{-1})
S0	0,89	3,30	2,53	395,25
S1	0,81	2,59	1,89	530,92
S2	0,76	2,56	1,78	563,06
S3	2,22	3,48	2,83	353,44
S4	0,78	2,51	1,81	550,02
S5	0,77	3,22	2,59	386,30
S6	1,08	3,53	2,58	387,2

CONCLUSION

The thesis, “*Perovskite $\text{Cs}_2\text{SnCl}_{6-x}\text{Br}_x$ ($x = 0, 1, 2, 3, 4, 5, 6$): Synthesis, Phonon Dynamics, and Optical Properties*” was conducted at the Institute of Materials Science, Vietnam Academy of Science and Technology. Partial results of the thesis have been published: 02 articles in SCIE journals (prestigious ISI); 01 article in a prestigious national journal in the scoring list of the State Professorship Council; and 01 national conference presentation.

Successfully fabricated double perovskite $\text{Cs}_2\text{SnCl}_{6-x}\text{Br}_x$ ($x = 0, 1, 2, 3, 4, 5, 6$) materials with micrometer-sized regions and good crystalline quality.

Calculated the phonon dispersion and density of states and experimentally measured the Raman scattering spectra of the fabricated material.

Calculated the electronic band structure and density of states of the double perovskites Cs_2SnCl_6 and Cs_2SnBr_6 , determining the direct band gaps of these crystals to be 3.56 eV and 2.93 eV, respectively. These results are in close agreement with the band gaps determined experimentally from absorption spectra. The band gaps of the $\text{Cs}_2\text{SnCl}_{6-x}\text{Br}_x$ ($x = 0, 1, 2, 3, 4, 5, 6$) materials were experimentally determined from absorption spectra.

Identified the mechanism of self-trapped exciton (STE) luminescence in the Cs_2SnBr_6 crystal involving a strong electron-phonon interaction, which leads to broadening of the fluorescence spectrum and a large Stokes shift.

Raman spectroscopy of the $\text{Cs}_2\text{SnCl}_{6-x}\text{Br}_x$ ($x = 0, 1, 2, 3, 4, 5, 6$) crystals revealed three characteristic vibrational modes: $\delta(\text{T}_{2g})$, $\nu(\text{E}_g)$, and $\nu(\text{A}_{1g})$. As x increased from 1 to 3, new Raman peaks appeared at 271.9 cm^{-1} , 263.6 cm^{-1} , and 252.5 cm^{-1} , near the $\nu(\text{A}_{1g})$ peak. Additionally, another peak appeared around 100.4 cm^{-1} . These Raman modes may be related to the short-range ordering of Cl^-/Br^- anions.

The band gap bowing of the halogen-substituted $\text{Cs}_2\text{SnCl}_{6-x}\text{Br}_x$ ($x = 0, 1, 2, 3, 4, 5, 6$) samples had a band gap bowing coefficient of $b = -0.12$. This demonstrates the rapid decrease in band gap energy as the Br content increases, reflecting the strong influence of Cl substitution by Br in the crystal structure.

RECOMMENDATIONS

Further exploration of doped Cs_2SnX_6 ($X = \text{Cl}, \text{Br}$) systems with elements such as Sb or Bi to investigate their optical properties and enhance photoluminescence quantum yield (PLQY).

Structural optimization of doped $\text{Cs}_2\text{SnCl}_{6-x}\text{Br}_x$ with extended Cl/Br ratios to identify the optimal composition for superior optical performance.

Trial fabrication of optoelectronic devices (such as perovskite solar cells - PSCs) based on the synthesized perovskite systems.

NEW CONTRIBUTIONS OF THE THESIS

Successfully fabricated double perovskite $\text{Cs}_2\text{SnCl}_{6-x}\text{Br}_x$ ($x = 0, 1, 2, 3, 4, 5, 6$) materials with micrometer-sized regions and good crystalline quality.

Calculated the phonon dispersion and density of states and experimentally measured the Raman scattering spectra of the fabricated material.

Calculated the electronic band structure and density of states of the double perovskites Cs_2SnCl_6 and Cs_2SnBr_6 , determining the direct band gaps of these crystals to be 3.56 eV and 2.93 eV, respectively. These results are in close agreement with the band gaps determined experimentally from absorption spectra. The band gaps of the $\text{Cs}_2\text{SnCl}_{6-x}\text{Br}_x$ ($x = 0, 1, 2, 3, 4, 5, 6$) materials were experimentally determined from absorption spectra.

Identified the mechanism of self-trapped exciton (STE) luminescence in the Cs_2SnBr_6 crystal involving a strong electron-phonon interaction, which leads to broadening of the fluorescence spectrum and a large Stokes shift.

LIST OF THE PUBLICATIONS OF AUTHOR

1. Anh Thi Le, Thanh Binh Dinh, T. Anh Thu Do, Truong Giang Ho, Duy Manh Le, Minh Tan Man, Lattice dynamics of double perovskite Cs_2SnCl_6 from first principles and experimental studies, *Materials Letters*, 309, 131386, (2022). <https://doi.org/10.1016/j.matlet.2021.131386> (Prestigious ISI-indexed journal).
2. Manh Ha Hoang, Duy Manh Le, Anh Thi Le, Quoc Khanh Nguyen, T Anh Thu Do, Truong Giang Ho and Minh Tan Man, Lattice dynamics and self-trapped excitons in the Cs_2SnBr_6 double perovskites, *Journal of Physics: Condensed Matter*, 36 (28), 285901, (2024). <https://doi.org/10.1088/1361-648X/ad3ac4>. (Prestigious ISI-indexed journal).
3. Le Anh Thi, Le Duy Manh, Do Thi Anh Thu, Ho Truong Giang, Man Minh Tan, Structural, Morphological, and Raman Spectral Characteristics of Cs_2SnCl_6 Double Perovskite Crystals, *Vietnam Journal of Catalysis and Adsorption*, 10(1), pp.108–111, (2021). <https://doi.org/10.51316/jca.2021.101>. (Reputable national journal)
4. Le Anh Thi, Le Duy Manh, Dinh Thanh Binh, Do Thi Anh Thu, Ho Truong Giang, Hoang Manh Ha, Man Minh Tan, Electron–Phonon Interaction and Self-Trapped Excitons in Cs_2SnBr_6 Double Perovskite Crystals, *Proceedings of the National Conference on Solid State Physics and Materials Science*, pp. 197–202, (2023).